Petroleum Science 21 (2024) 87–99

Contents lists available at ScienceDirect

Petroleum Science

journal homepage: www.keaipublishing.com/en/journals/petroleum-science

Original Paper

Geometry and formation mechanism of tension gashes and their implication on the hydrocarbon accumulation in the deep-seated strata of sedimentary basin: A case from Shunnan area of Tarim Basin

Yan-Nan Du [a], Kong-You Wu [a, *], Yin Liu [a, **], Yan-Ying Li [a], Zi-Cheng Cao [b], You-Wei Cui [c], Jun Liu [b]

[a] Key Laboratory of Deep Oil and Gas, School of Geosciences, China University of Petroleum (East China), Qingdao 266580, Shandong, China
[b] Exploration and Development Research Institute, SINOPEC Northwest Oilfield Branch, Urumqi 830011, Xinjiang, China
[c] The Fifth Gas Production Plant, Changqing Oilfield, PetroChina, Xi'an 710018, Shaanxi, China

ARTICLE INFO

Article history:
Received 13 July 2022
Received in revised form
8 May 2023
Accepted 25 October 2023
Available online 28 October 2023

Edited by Jie Hao and Teng Zhu

Keywords:
Tarim Basin
Sigmoidal tension gashes
Seismic attributes
Shear stress calculation
Formation mechanism
Reservoir control

ABSTRACT

With the theoretical and technological developments related to cratonic strike-slip faults, the Shuntuoguole Low Uplift in the Tarim Basin has attracted considerable attention recently. Affected by multi-stage tectonic movements, the strike-slip faults have controlled the distribution of hydrocarbon resources owing to the special fault characteristics and fault-related structures. In contrast, the kinematics and formation mechanism of strike-slip faults in buried sedimentary basins are difficult to investigate, limiting the discussion of these faults and hydrocarbon accumulation. In this study, we identified the characteristics of massive sigmoidal tension gashes (STGs) that formed in the Shunnan area of the Tarim Basin. High-resolution three-dimensional seismic data and attribute analyses were used to investigate their geometric and kinematic characteristics. Then, the stress state of each point of the STGs was calculated using seismic curvature attributes. Finally, the formation mechanism of the STGs and their roles in controlling hydrocarbon migration and accumulation were discussed. The results suggest that: (1) the STGs developed in the Shunnan area have a wide distribution, with a tensile fault arranged in an *en échelon* pattern, showing an S-shaped bending. These STGs formed in multiple stages, and differential rotation occurred along the direction of strike-slip stress during formation. (2) Near the principal displacement zone of the strike-slip faults, the stress value of the STGs was higher, gradually decreasing at both ends. The shallow layer deformation was greater than the deep layer deformation. (3) STGs are critical for connecting source rocks, migrating oil and gas, sealing horizontally, and developing efficient reservoirs. This study not only provides seismic evidence for the formation and evolution of super large STGs, but also provides certain guidance for oil and gas exploration in this area.

1. Introduction

Strike-slip faulting is highly developed in the Earth's crust, and various types of structures can form during faulting under stress fields, such as restraining bends, releasing bends, horsetail splay, and flower structures (Mann, 2007; Xu et al., 2011; Li et al., 2021), which reflect complex kinematic and dynamic backgrounds (Woodcock and Fischer, 1986; Dooley, 1994; Cembrano et al., 2005; Fossen, 2010). Among them, sigmoidal tension gashes (STGs) are tensile fractures with special geometric shapes developed by shear stress and act as an efficient sign for investigating the kinematic environment (Lisle, 2013). Horizontally, several STGs are usually assembled along the shearing direction, exhibiting an *en échelon* pattern. Vertically, the cross-section of an STG has an "S" or "reverse-S" shape, which is thicker in the middle and thinner at both ends (Lajtai, 1969; Lisle, 2013). In addition, other shear deformations appear with the development of STGs (Lisle, 2013). Most tension gashes are well observed in outcrops with scales of several centimeters or meters (Rispoli, 1981; Lisle, 2013; Emese et al., 2019). However, the identification of tension gashes in buried

* Corresponding author.
** Corresponding author.
E-mail addresses: wukongyou@163.com (K.-Y. Wu), liuyin@upc.edu.cn (Y. Liu).

https://doi.org/10.1016/j.petsci.2023.10.021

strata is limited owing to the restrictions of research methods and formation mechanism constraints. In this study, we identified the massive STGs that developed in the buried sedimentary strata from the Upper Ordovician to Silurian in the Shunnan area of the Tarim Basin. These tension gashes can span several kilometers, as clearly evident from the seismic data. Previous studies have suggested that these strike-slip related structures are formed by the upward divergence and transmission of tensile and torsional stresses (Jiao, 2017). Small grabens were generated owing to pull-apart extension along the strike-slip faults (Wang et al., 2014a; Deng et al., 2018a). However, the special characteristics shown by seismic data reflect that the formation of these structures occurred under more complex stress environments.

The Tarim Basin covers an area of approximately 400, 000 km^2 and continues to attract the attention of researchers as the largest inland basin in China. Exploration indicates that the amount of oil and gas resources within the basin is 1.21×10^{10} tons and 1.47×10^{13} m^3, respectively (Kang, 2018). Since 2014, petroleum exploration has exposed a genetic link between strike-slip faults and hydrocarbon accumulation in the presence of several large hydrocarbon reservoirs in this area (Jiao, 2018; Han et al., 2019; Lin et al., 2021; Jia et al., 2021; Wang et al., 2021; Wang et al., 2021). However, the evolution and formation of these strike-slip faults remain debatable. The strike-slip fault has complex structural characteristics on the plane, and the fault displacement is not obvious on the profile. This feature makes seismic identification unclear and influences the studies about the formation mechanism. (Qi, 2016; Han et al., 2018; Deng et al., 2018b). By using high-resolution three-dimensional (3D) seismic data and related analysis, we identified the massive tension gashes in the Shunnan area of the Tarim Basin. The aims of our study included (1) revealing the kinematic history of the strike-slip faults in the Shunnan area; (2) discussing the formation mechanism of these tension gashes; and (3) providing a view on the relationship between strike-slip faults and hydrocarbon accumulation. This study is not only important in defining the development scale and geometric configuration of the STGs but also helpful for hydrocarbon exploration in similar areas.

2. Geological setting

The Shunnan area, also known as the southern part of the Shuntuoguole Low Uplift, is located along the northern slope of the Tazhong Uplift. It is adjacent to the Manjiaer Depression to the east and the Tazhong Uplift to the southwest (Fig. 1a–b) (Li et al., 2017; Liu et al., 2021). A series of strike-slip and tensile secondary faults have developed in the Shunnan area. These strike-slip faults can be divided into three groups, NE- and NEE-trending, and the tensile secondary faults that are mainly NNW-trending (Fig. 1c). On the fault plane distribution figure (Fig. 1c), the strike of these faults is relatively straight and NE-and NEE-trending strike-slip faults show an “X”-pattern. The scales of these faults differ. Among them, the NE-striking strike-slip faults are usually large, cutting through the Upper Paleozoic and merging into the basement. The SN-3, SN-1, SN-4, and SN-2 faults are distributed successively from west to east. Compared with the NE-trending faults, the scale of the NEE-striking strike-slip faults is relatively small, and most are constrained in the sedimentary cover (e.g., SN-5 Fault). The NNW-striking faults are mostly small-scale branches formed during the main strike-slip faulting. They are mainly distributed in the overstepped zones of the NE- and NEE-trending strike-slip faults and developed during the Upper Ordovician and Silurian (Zhang et al., 2018). The evolution of the Shunnan area experienced multiple stages of tectonic activity (Yun and Cao, 2014; Zhen et al., 2015; Zhu et al., 2016). Based on the previous studies on the occurrence time of peripheral orogeny in different stages of the Tarim Basin, the Shuntuoguole Low Uplift, where the study area is located, is a product of the coupled superposition of the clockwise drift of the Tarim Plate and the counterclockwise closure orogeny (Han et al., 2018; Qiu et al., 2019). In the middle of the Caledonian movement, the Kunlun Massif collided with the Tarim Plate at the earliest, and the collision lasted from the Cambrian to the early Silurian. The Tazhong Uplift and Shuntuogole Low Uplift were formed in the foreland basin system in the direction of the southwest sag. The southern part of the Shuntuogole Low Uplift is located in the outer uplift depression of the foreland basin and is affected by the NE-trending transpression stress field, forming a NE-trending strike-slip fault system (Liu et al., 2023). During this period, the Altyn Block in the southeastern part of the basin also collided with the Tarim Plate, and the collision lasted from the Cambrian to the Devonian, forming the Altyn foreland basin system. Therefore, the southern part of Shuntuoguole was also affected by the superposition of the NNW transpression stress field during the Caledonian movement. The collisional merging of the Tian Shan massif and the Tarim Plate occurred in the Hercynian, forming a foreland basin system at the northern edge of the Tarim Basin. At this time, the northern Tarim Uplift was strongly uplifted, and the low uplift of Shuntuoguole,

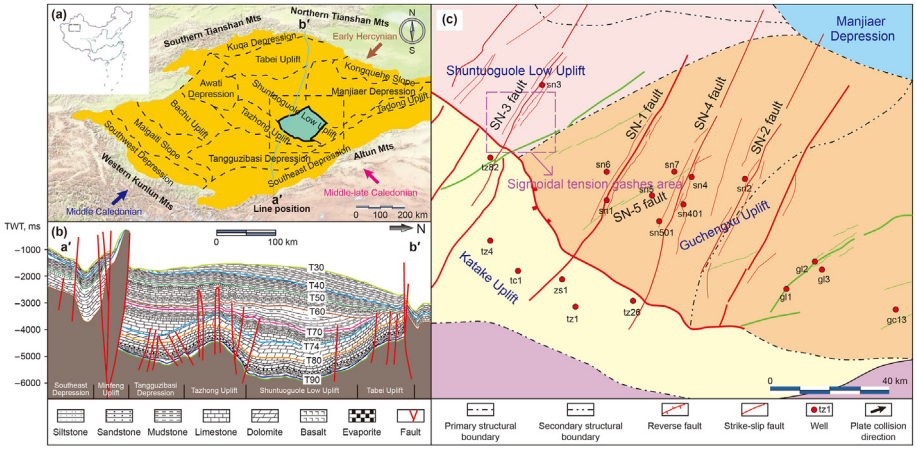

Fig. 1. Sketch maps. (a) Showing the tectonic location of the Shunnan area in Tarim Basin and the location of the measured lines in profile (b). (b) Showing the tectonic features of the north-south profile cutting through the study area, showing the main lithological features of the layers and the boundaries of the tectonic units. (c) Showing the boundaries of the tectonic units in the study area, the distribution and names of the major faults, and well locations (modified after Wang et al., 2022).

located on its southern slope, was subjected to the NE-SW compression-torsional stresses, with inherited development of a strike-slip fracture system. During the Late Hercynian-Indosinian, the South Tianshan Block collided with the Tarim Plate, and the Shunnan area continued developing at the slope background with the activities of the strike-slip faults. From the Yanshanian to the Himalayan, the tectonic influence on the Shunnan area was weak, and some of the previous strike-slip faults were reactive (Qiu et al., 2019; Liu et al., 2023).

In terms of profile characteristics, there are at least two stages of strike-slip faults in the study area. The early strike-slip faults cut through the T_8^0–T_7^4 reflecting layer, showing vertical linear or positive flower structures on the profile (Fig. 2), indicating a compressive torsional stress environment, which was formed in the middle late Caledonian tectonic movement (He et al., 2005; Zhu et al., 2016). The late strike-slip fault cuts through the T_7^0–T_6^5 reflecting layer, showing a negative flower structure (STG) on the profile (Fig. 2), indicating a tensional torsional stress environment, which was formed during the early Hercynian tectonic movement (Zhao and Jia, 2002; Yun and Cao, 2014).

The sedimentary strata were well-developed in the Tarim Basin, and the total thickness of the strata exceeded 10 km. From the Cambrian to Ordovician, the basin was mainly characterized by a carbonate platform with the deposition of carbonate rocks, including limestone and dolomites (Tang, 1994; Li et al., 2017). The Cambrian strata were relatively gentle and unconformable above the Precambrian basement. They mainly comprised gray dolomite, with a small amount of dark gray mudstone and purple gypsum (Han et al., 2018). The Ordovician is well-developed and in integrated contact with the underlying Cambrian. In the Shunnan area, the carbonate platform facies include the Lower Ordovician Penglaiba Formation to the Middle Ordovician Yijianfang Formation, and the lithology gradually transitions from dolomite to limestone. The Upper Ordovician is composed of thick shelf deposits, and the lithology is mainly limestone, argillaceous limestone, and mudstone (Yun and Cao, 2014). From the Silurian to the Middle Devonian, terrigenous clastic rocks of coastal shallow marine facies, including graywackes, argillaceous siltstones, sandstones, mudstones, and shales were deposited in the area (Ren et al., 2011). The Upper Devonian deposited fine coastal sandstone facies with an

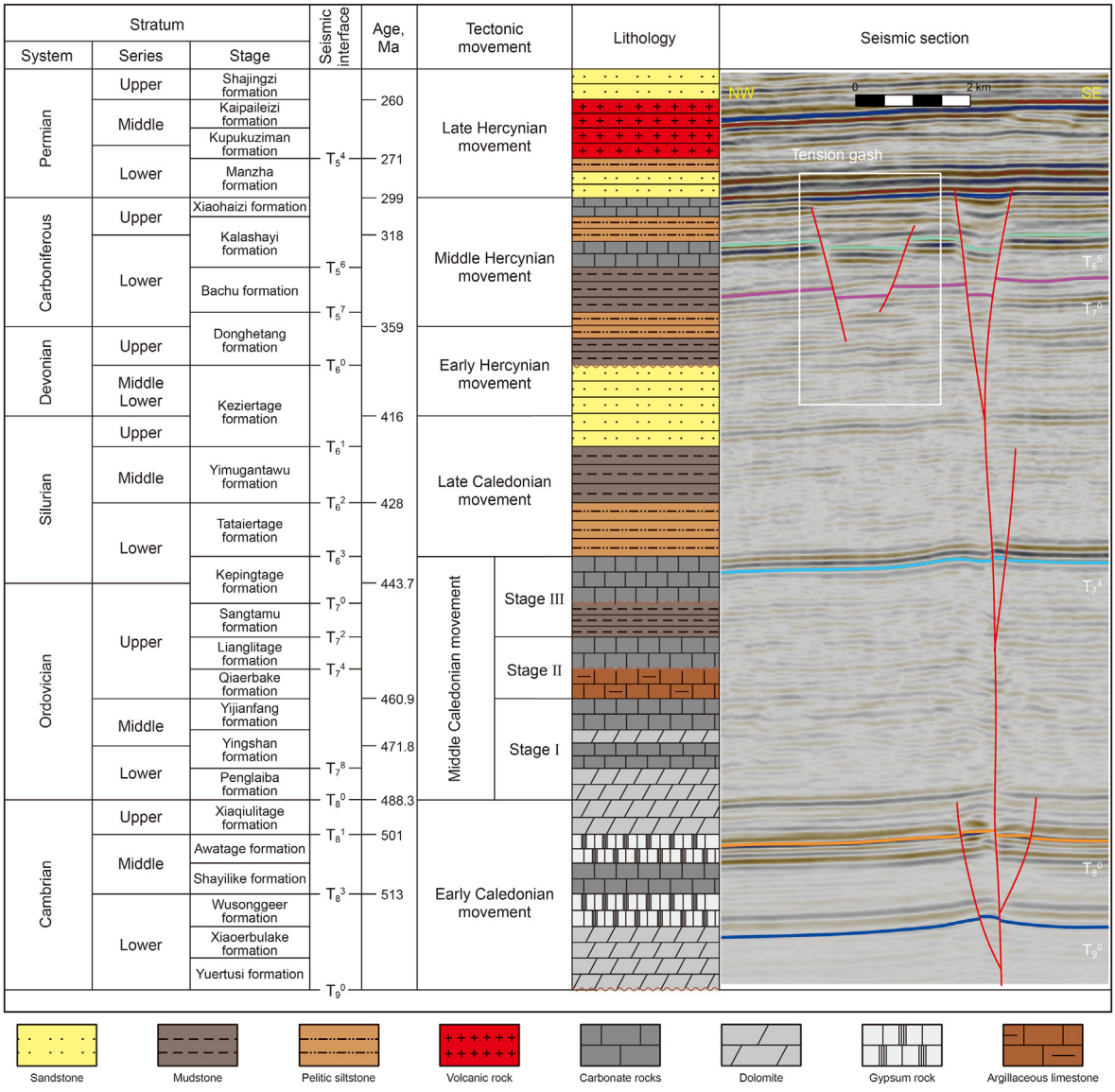

Fig. 2. Geological age and lithology of Shunnan area, Tarim Basin (modified after the SINOPEC Northwest Oilfield Company; Zhen et al., 2015).

angular or parallel unconformity developed at its top and bottom (Han et al., 2018). The Carboniferous is composed of clastic rocks and carbonate deposits from an open-platform environment, leading to an unconformable contact with the underlying Donghetang Formation. A gap exists between the middle-lower Permian and Carboniferous strata, the top of which is a regional unconformity. The lithology of the Carboniferous is dominated by sand-mudstone deposits from alternating marine, continental, and river facies (Yun and Cao, 2014). The bottom of the Upper Permian is unconformable to the Carboniferous, and the top is truncated by another unconformity. The lithology of the Upper Permian is continental coarse clastic rock deposits.

3. Data and methods

3.1. Data source

3D seismic surveys were conducted covering 330 km^2 of STGs. Our high-resolution 3D datasets provided better identification of complex tectonic systems. This is clearer in the wave group characteristics of the carbonate rock layer system, which develops STGs with a high signal-to-noise ratio, good reflection, and strong continuity. The seismic data use time-domain datasets without time-depth conversion, which can reflect the most original tectonic features. The transverse wave velocities of the Ordovician formations in the Shunnan area range from 2922 to 3130 m/s (Wang et al., 2014b), with slight differences in velocities between different lithologies. The main frequency of the seismic waves is between 16 and 23 Hz. The average vertical resolution was calculated as between 34 and 45 m. The calibration of seismic layers and major reflectors was based on studies by the Northwest Oilfield Company, Sinopec. To describe the STGs, we intercepted eight seismic profiles, cutting different parts of the tension gashes for a detailed seismic interpretation.

3.2. 3D seismic interpretation

In terms of static correction, denoising, and pre-stack migration, the presentation quality of 3D seismic datasets has greatly improved, and structural features previously overlooked can now be seen more clearly. In blocks with complex geological conditions, multiple faults are staggered, and multiple types of faults develop together. There are several methods for interpreting faults, however the relationship between the main and secondary faults remains unclear. The ability to dissect seismic data from multiple directions and perspectives with 3D seismic interpretation significantly reduces the risk of misjudging fault development and the nature of their strikes arising when interpretations are made based on a single perspective. The development of NE-trending strike-slip faults and the associated NNW-trending STGs have different tendencies, and the strike of the STGs twists in the plane near the main shear displacement zone. These faults have different seismic responses to data received from different directions, owing to their different strikes and tendencies.

The seismic interpretation was performed on the Petrel Platform. The stratigraphic data were calibrated using well data provided by the Northwest Oilfield. Seismic profiles were selected at equal distances (100 traces apart) in the inline and crossline directions of the datasets for seed point interpretation. The layers were interpreted in a 3D space using Petrel's automatic seed point tracking function. Then, 3D stratigraphic tracking was performed on the smoothed seismic datasets, clarifying the fault display and ensuring that the structure was undeformed. For parameter selection, the seed point tracking provides amplitude and proximity. The quality selection was validated as 5×5 to provide better clarity. Based on the attitudes of the stratum, we selected dip-tracking ranges of 5 and 4 ms in the inline and crossline directions, respectively. The correlation coefficient between the tracked and seed points was 0.7. Then, the tracked horizon interpretation data were used to generate the surface, which was then superimposed with the seismic attribute to obtain the surface attribute and provide the basis for fault interpretation.

In terms of fault interpretation, Petrel supports fault tracking from multiple directions, largely avoiding fault interpretation errors and improving the accuracy of the interpretation. During the interpretation, we modeled the fault; therefore, we could correct the interpretation results. For seismic interpretation of complex structural zones, we used seismic attributes such as dip angle, curvature, and amplitude to assist and accurately describe fault morphology.

3.3. Seismic attribute analysis

The shear stress of the main displacement zone influences the development of the STGs, resulting in complex structural deformation. The response characteristics of seismic data to faults can be improved using attribute analysis, and the structural characteristics of complex areas can be described more accurately.

The ant tracking method was used in this study to recognize STGs under multiple attribute constraints. The ant-tracking method is a bionic technology based on the ant algorithm proposed by Dorigo et al. (1996). Ant-tracking technology searches for fracture traces in seismic data volumes until fault tracking and identification are completed, based on the principle that ants use secretions to find food sources as quickly as possible (Wang et al., 2013; Zhou et al., 2015). This tracking technology can highlight seismic data discontinuities, strengthen new attributes of fracture characteristics, improve fracture prediction accuracy, and enrich geological structure details. To create the ant-tracking datasets, we used a comprehensive method based on the following workflow: smoothing the original seismic data volume, reducing the influence of noise, and improving the consistency of the seismic effective reflection. Then, to improve fault continuity, discontinuity is detected using the dip angle and curvature attributes. Owing to the complex tectonic setting of the Shunnan area, the faults were predominantly NW- and NE-trending. As a result, the active mode was chosen from the two combined modes of the tracking parameters provided by the Petrel Platform. The initial ant boundary was smaller in this mode, the search threshold value was larger, and the "ants" were better at finding faults and depicting fracture details.

3.4. Shear strain calculation

The passive rotation mode in a two-dimensional plane can be used for strain analysis of the shear zone. The passive rotation mode of STGs assumes that the curvature has a nonuniform strain effect in the shear zone, resulting in differential rotation in different parts of the tension gash. The degree of deformation for each part of the fracture was determined by its initial direction and cumulative strain at that location (Lisle, 2013). The initial fracture direction was determined by the type of fracture in simple shear mode. Different types of fractures were distinguished based on their direction (Beach, 1975). The angle between the tension gash formed by simple shear and the main slip zone was approximately 45°; however, when positive and negative volume variables were present, the angle changed (Ramsay and Graham, 1970).

In the absence of information regarding the original fracture direction, an estimated value can be obtained from the direction of the fracture tip at the edge of the shear zone. This method assumes

that the shear strain gradient at the boundary changes over time.

The shear strain at each point in the STG can be expressed by the variation in the initial direction of the fracture and the tangent direction of each point. It is calculated using the equation given by Ramsay and Huber (1983):

$$\gamma = \cot \alpha - \cot \alpha' \quad (1)$$

where α represents the angle between the initial direction of the fracture and the shear zone, and α' represents the angle between the tangential direction of each point on the STG after deformation and the shear zone (Fig. 3a).

According to Eq. (1), γ represents the local shear strain in the STG and reflects the variation in the overall stress gradient. γ_m represents the average value of γ in the STG, reflecting the deformation degree of the STG as a whole. As depicted in Fig. 3a, the simulation shows that higher γ_m values lead to a greater deformation degree of the STG. The shear strain at both ends of the STG had a high variation gradient and gradually increased toward the center, reaching the maximum at the center.

The strain distribution of the shear zone controls the STGs geometry. Several theoretical models have been proposed for the distribution of strain and displacement characteristics in the evolution of the shear zone (Means, 1984, 1995; Vitale and Mazzoli, 2008; Fossen and Cavalcante, 2017). The idealized model can explain the morphological differences in the STGs along the shear zone. The strain distribution characteristics of the shear zone can also be analyzed by calculating the strain values at each point of the STGs. The initial deformation of Type 1 occurred at the center, and the strain was gradually displaced to both ends over time. A box shape was observed in the strain value curve (Fig. 3b). The strains exhibited high rates of change at both ends and remained constant in the center. Conversely, the strain of Type 2 gradually accumulated towards the center, where the strain value was abnormally high (Fig. 3b). Type 3 model maintained a constant strain range, with strain occurring at the boundary of the deformation range. The strain range of Type 4 increased gradually over time. In contrast to Type 1, Type 4 maintained a continuous process of change at the center. The curve shows a continuous increase in strain rate (Fossen and Cavalcante, 2017).

4. Results

4.1. Plane development characteristics of tension gashes

STGs developed in the Silurian-Ordovician strata in the Shunnan area, with a burial depth of more than 3500 m, belonging to deep-seated faults and unable to be directly observed. Using the 3D seismic data and corresponding ant-tracking dataset, the geometric characteristics of STGs were analyzed both horizontally and vertically (Fig. 4). Our observations indicate that the STGs developed in the SN-3, SN-1, and SN-4 faults. The STGs of the SN-3 fault are described in detail. Five groups of NW-trending STGs were arranged in parallel in the stratum from −2850 to −3550 ms (time domain), with an azimuth of 340 ± 2° and an extension of 5–15 km. A group of *en échelon* pattern faults developed in the NE direction, cutting into or through the NW-trending STGs with an azimuth of 20–30° and an intersection angle of approximately 40–55°. The intersection relationship showed that the development times of the two fault groups had an obvious sequential relationship.

In plan view, STGs typically have two spindle-like faults (STG-1, STG-2, STG-4, and STG-5); however, the single fault (STG-3) is also present. When the STGs having different numbers of faults are compared, those with a single fault are cut more easily by paired NE-trending faults. An STG with two faults is not prone to dislocation and exhibits only tangential deformation and cutting-in characteristics. When the NE-trending strike-slip fault intersects STG-1 and STG-3, it exhibits the symbiotic characteristics of the two faults, which differ from those of the traditional *en échelon* strike-slip faults. "S" bending of STGs occurs near the main strike-slip displacement zone, and their bending protrusion direction is consistent with the rotation of the strike-slip fault, indicating the

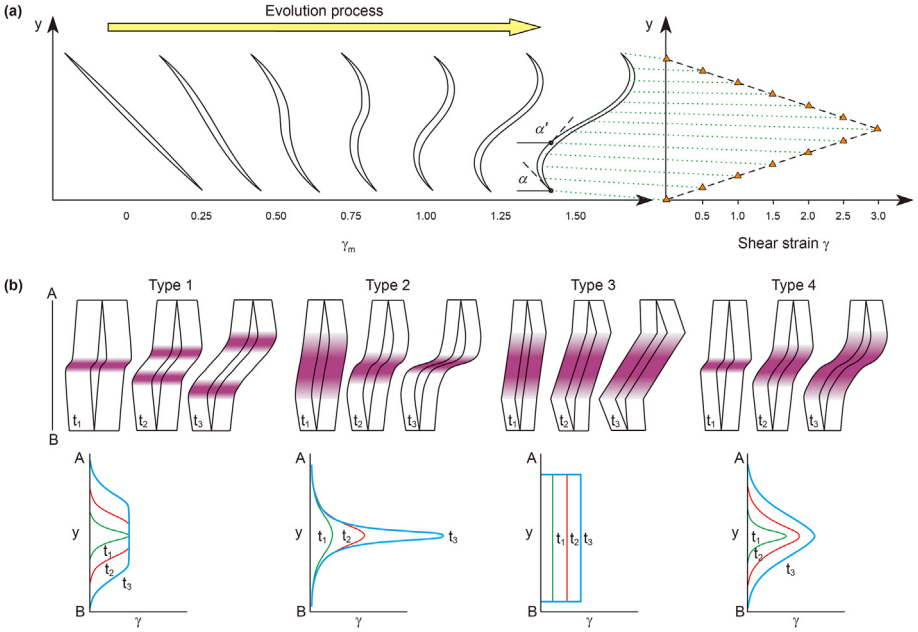

Fig. 3. Sigmoidal tension gashes produced by heterogeneous simple shear and four different types of shear zones based on deformation and activity through time. (a) Progressive evolution of gash shape with increase in the average shear strain across the shear zone and simulation of the strain gradient at each point of the sigmoidal tension gashes (modified after Lisle, 2013). (b) Four idealized models, where the purple-red fields represent the active part of the shear zone. The shear strain gradient across the boundary variables correspond to each type one by one (modified after Fossen and Cavalcante, 2017).

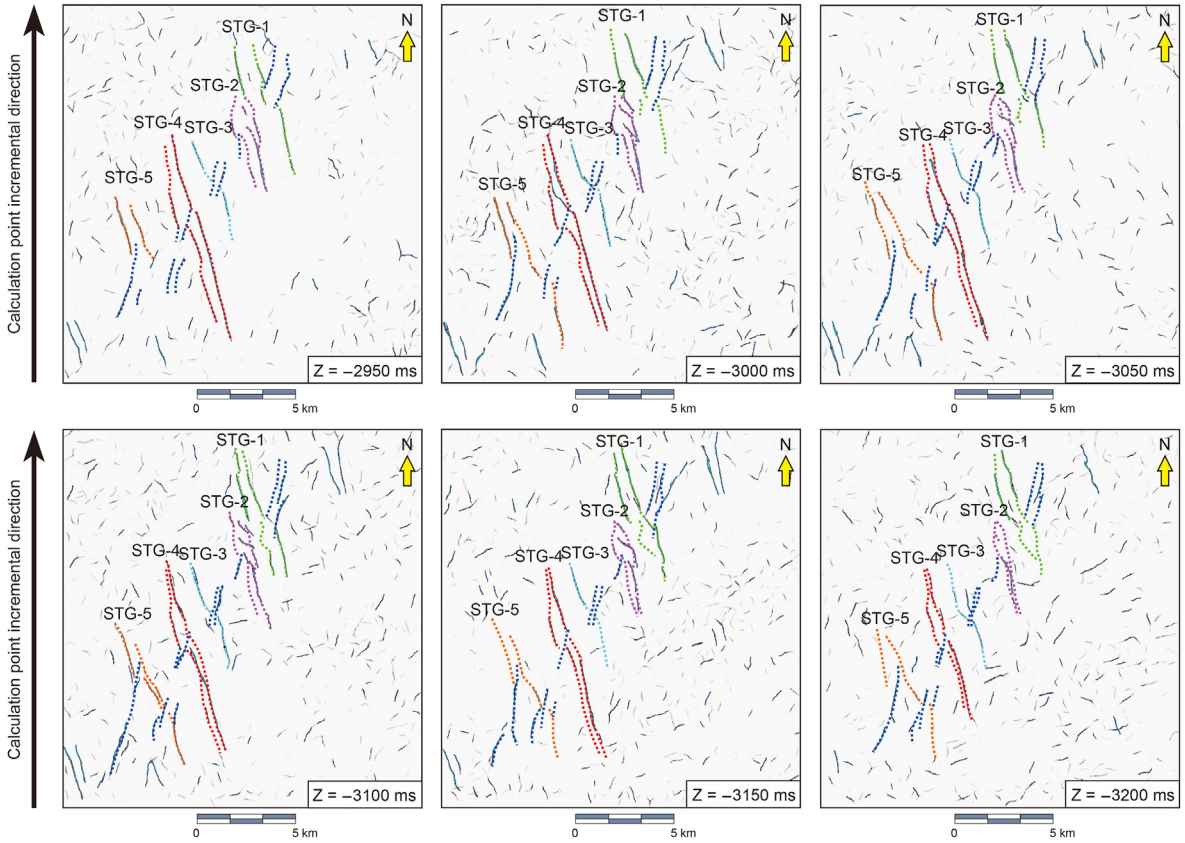

Fig. 4. Horizontal slices of the ant-tracking data volume at 2950, 3000, 3050, 3100, 3150, 3200 ms, and the plane interpretation of sigmoidal tension gashes.

direction of the shear stress field.

4.2. Fault development characteristics on seismic sections

As shown in Fig. 5, the formation of STGs is controlled by the SN-3 fault. The section of the SN-3 fault exhibits a transpression positive flower structure in the early stage (first stage of the Middle Caledonian) and layered superposition of transtension negative flower structure in the late stage due to the superposition effect of multi-stage tectonic movements (second stage of the Middle Caledonian). The SN-3 fault was inherited and developed during the Late Caledonian-Early Hercynian tectonic movement, displaying an *en échelon* pattern in the plane view and a negative flower structure in the cross-sections.

STGs are characterized by tensional structures in their cross-sections. A large-scale STG is composed of two fault branches

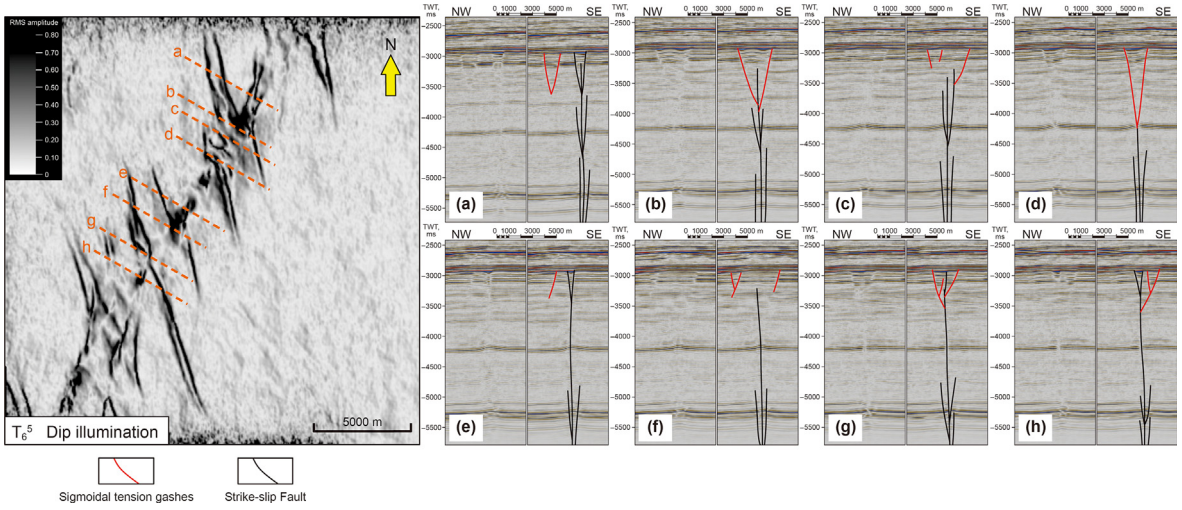

Fig. 5. Seismic cross-section across the sigmoidal tension gashes (northwest direction) of SN-3 Fault. It contains both original and interpreted profiles. The dip illumination attribute surface of T_6^5 horizon is adopted in the plan.

with opposite dips (Fig. 6a). One branch has a large fault displacement and plays a dominant role in the development of the STGs, and the other is an associated branch (Fig. 6a). In the cross-sections, the structural style of the STG is Y-shaped or graben-like (Fig. 5a and c). A smaller STG appears in the form of a platy normal fault (Fig. 5e). After comparing the seismic profiles at different locations, the STGs were found to have the following characteristics: (1) Closer to the principal displacement zone (PDZ) of the strike-slip fault, the fault distance and width of the STG are greater, and it is connected with the strike-slip fault, forming a negative flower structure (Fig. 5b and d). (2) At the intersection of the strike-slip fault and STG, the strike-slip fault may not develop (Fig. 5d) or only develop as a shear fault (Fig. 5b and g) (weak discontinuity of reflectors on the two sides of the fault) in the shallow layer (Silurian). However, when the STG is far from the PDZ, the strike-slip fault cuts upward through the shallow strata and develops a negative flower structure (Fig. 5a and e) with obvious transtension characteristics, differing from typical *en échelon* strike-slip faults.

5. Discussion

5.1. Strain characteristics of sigmoidal tension gashes

To describe the strain characteristics of the STGs in space, we established the model of each fault through seismic interpretation of the section (Fig. 6b). In Petrel, the fault models were superposed with six isochronous slices to explain the plane boundary of each fault. In the slice, a uniform grid line was created. The direction of the grid line was parallel to the direction of the initial fracture of the STG (obtained by measuring the strike of the two endpoints of the gash). The angle between the tangent line of the measuring point and the grid line was α. The strain of each point was calculated by this method. A total of 360 measurement points were used. During the measurement, the shear zone direction was determined by the regional stress field, and the early strike-slip fault strike direction, and initial development direction of STGs were determined by the strike of the fault tip and that of the late tension fault.

The strain value initially increased and then decreased (Fig. 7). The overall shape of the curve (Fig. 7) indicates that the calculated results were roughly similar to those of Type 2 in Fig. 3b, with the high strain band concentrated in the center of the STG. The high-strain zone overlaps with the displacement zone of the early strike-slip fault and is the main location where the local fault strike of the STG rotates (Dooley and Schreurs, 2012). However, the local curve characteristics show that the calculated results also differed from those of Type 2, and there are relatively high zones in the process of the γ value change from the tips of the STG to the center (Fig. 7). This phenomenon is found in different time slice. Considering the stress distribution, several small shear stress zones were presumably present inside the shear zone in addition to the main displacement zone. The location and size of the STG in the shear zone also affected its strain curve. For example, STG-3 had a smaller fracture scale than STG-1 and STG-4. Only a single peak was observed in the strain curve, and the slices showed a typical S-shaped characteristic. However, larger STGs tend to exhibit more complex shapes. The different locations of STG in the shear zone caused a difference in the degree of the strain occurring at its two tips, resulting in the asymmetry of the strain curve (Fig. 7, STG-2 and STG-5).

According to the method presented in Section 3, the value of average shear strain (γ_m) can indicate the degree of deformation of an STG as a whole. Then, the deformation characteristics of the STG in space can be explored by comparing the γ_m values of the STG in the same and different time slices. Based on the data analysis in Fig. 8, the deformation degree of the STG gradually increased from the NE to SW in the same time slice. This phenomenon is likely related to the NE shear stress caused by the thrust and extrusion of the Tazhong I fault in the southwest of the study area. The closer it is to the thrust zone, the stronger the shear stress. By comparing the different time slices γ_m, it can be observed that the deformation degree of the STG was uneven in the longitudinal direction. With an increase in depth, it first increased and then decreased. In the time domain from −3050 to −3150 ms, the deformation degree of each STG was the largest. This phenomenon can indicate the evolution characteristics of the regional shear stress in time and space.

5.2. Formation mechanism

The formation of the STG is primarily controlled by the shear stress field in the study area and is inherited from the development of the early strike-slip faults. The shear stress (σ) can generate two

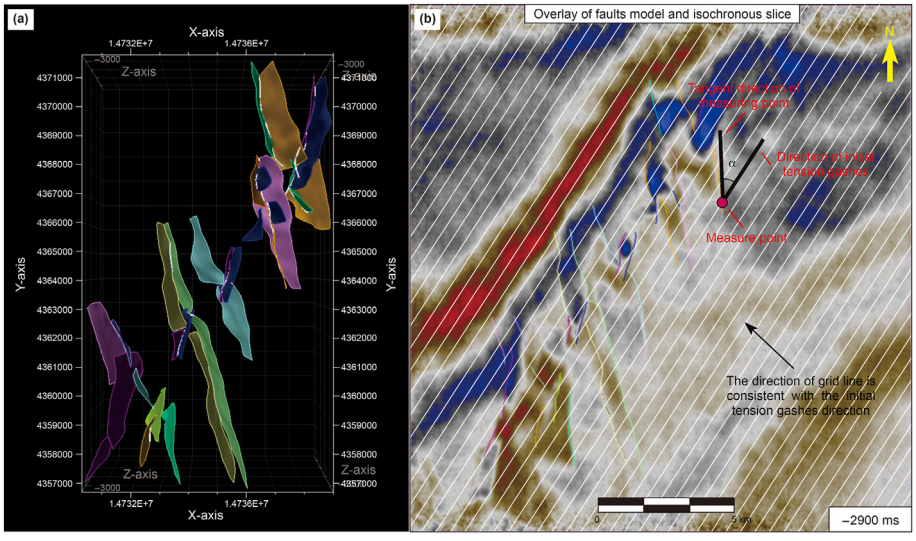

Fig. 6. 3D model of sigmoidal tension gashes and schematic diagram of measuring grid. (a) Using petrel modeling technology to establish STG faults model. (b) Establish the measuring grid on the fracture model and isochronous slice to prepare for measuring the strain value at each point of STG.

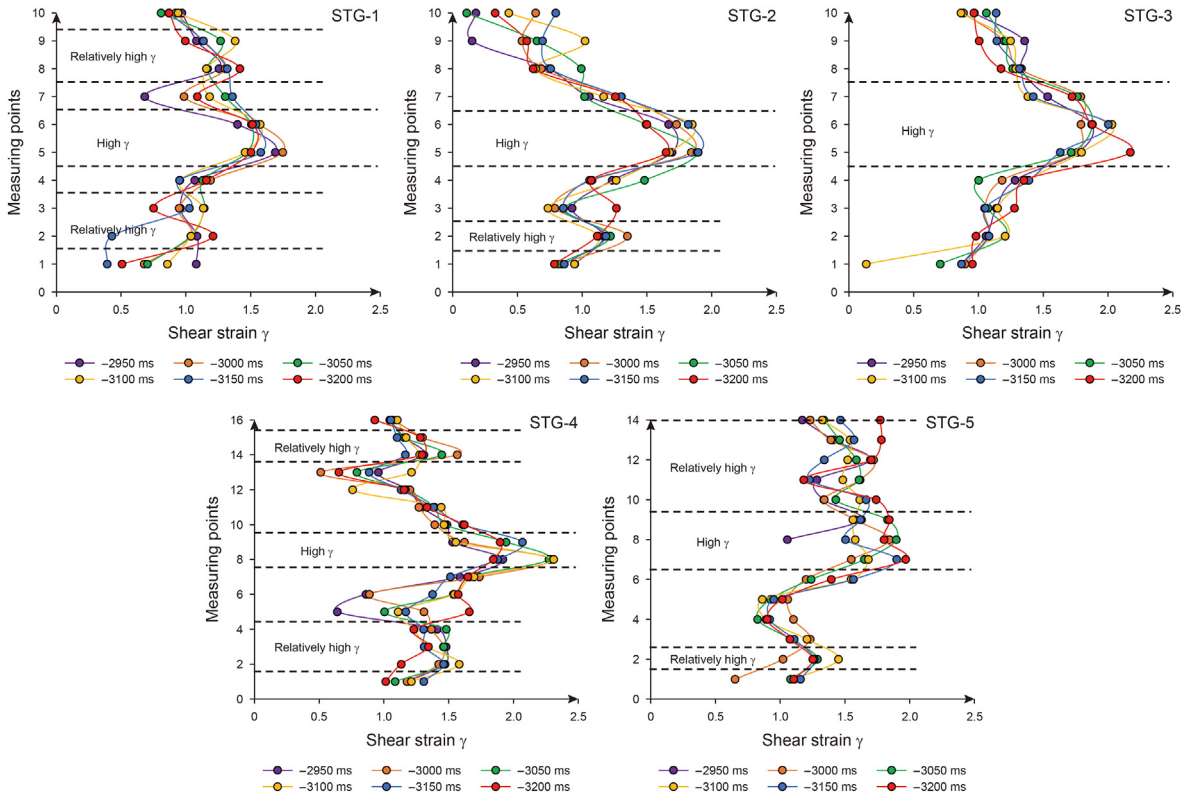

Fig. 7. Calculation of the shear strain value (γ) at the points along the STGs edge in the shear zone. The calculation method uses Eq. (1). The measured data were obtained by Fig. 4.

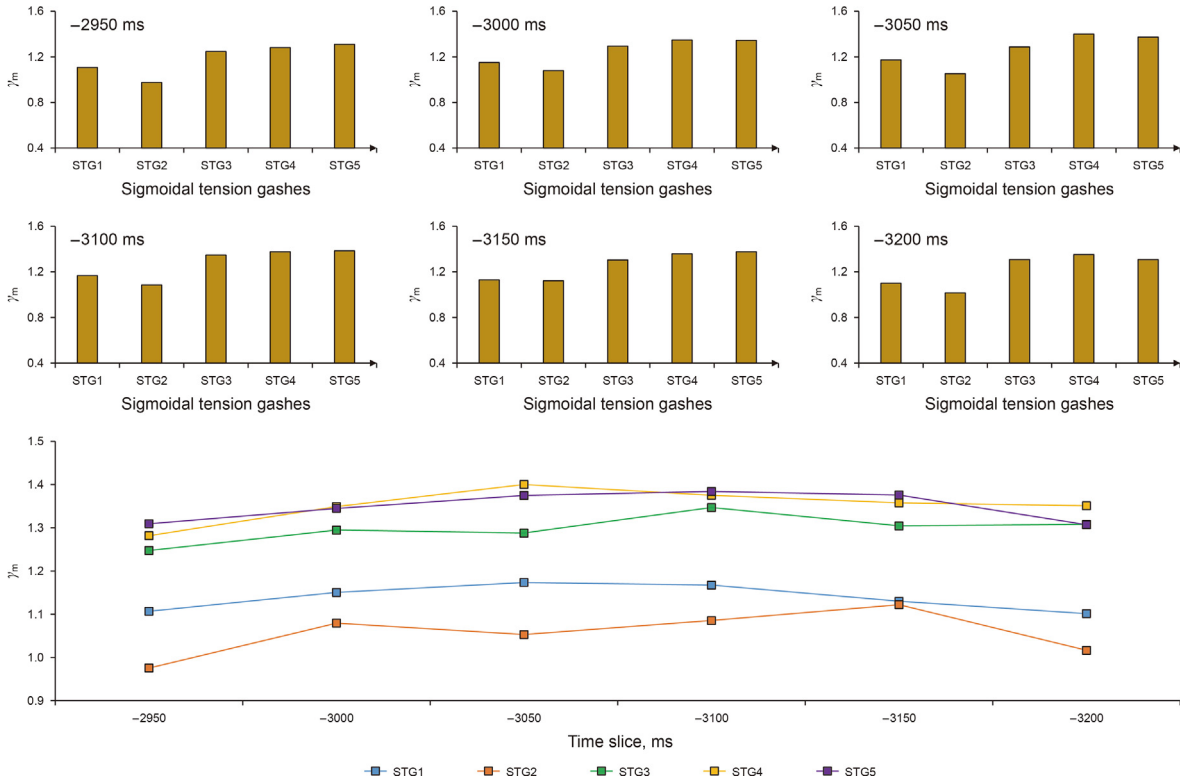

Fig. 8. Statistics of average shear strain (γ_m) for each STG in different time slices. The statistics are obtained by the calculation in Fig. 7. The average shear strain can indicate the strength of the overall STG activity.

components, σ_1 and σ_3, which are perpendicular. The interaction of these two components generates the early tensional fault of STG. As shown in Fig. 9a, when the block is affected by two shear stresses in opposite directions, their respective stress components (σ_1) move together, causing extrusion along the diagonal line. In contrast, the other stress component, σ_3 moves in the opposite direction and produces tensile stress along its diagonal line. The interaction between the two stresses results in a tensile fracture with a shear zone at a 45° angle. The fracture surface expands and grows as the shear stress intensity increases, forming an early tension gash.

Smith and Durney (1992) have performed physical experiments on clay models with fractures under different shear stress directions by changing the displacement direction of the shear zone to observe the strike of the derived fractures. The changing trend of the strike of expansion fractures is shown in Fig. 10. The direction of the expansion fractures changes with the displacement direction of the shear zone and is parallel to the principal stress (σ_1) direction. This is consistent with the stress mechanism of STG initial tension gashes described above.

The initial tension gashes begin to grow and extend with an increase in shear stress. Due to the angle between the strike of the tension gashes and the PDZ, the distance between the points on the tension gash and the core of the PDZ is different. Some scholars have studied the distribution of stress magnitude within the range of strike-slip fault periphery by means of stress field numerical simulation, fracture density identification, stress state measurement of rock and others (Huang et al., 1998; Shen et al., 2008; Liu et al., 2023). The results showed that the stress field around the large strike-slip fault varies in gradient. Taking the major principal stress distribution as an example, the stress value at the core of the PDZ is small. With the distance from the core gradually increasing, the stress value first increases and then decreases. Therefore, under the control of gradient stress field, the magnitude of stress at each point on the initial tension gash is different, and the resulting strain displacement distance is also different (consistent with the measured results in Fig. 7). This phenomenon is characterized by rotation on the macrography.

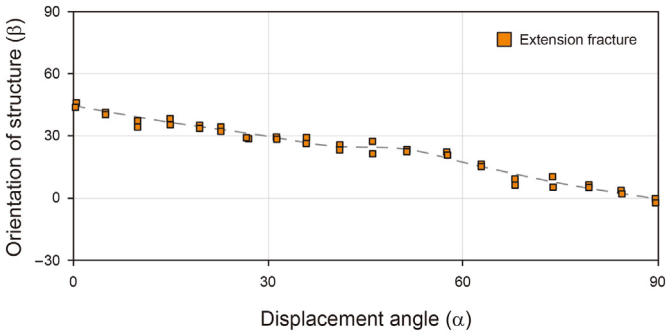

Fig. 10. Graphical representation of the experimental results showing the orientation of extension structures. The data in the figure is derived from the experimental measurement results of Smith and Durney (1992) clay model. The experiment observed the variation of the strike of the derived fault by changing the azimuth of the shear displacement zone. This figure only selects the displacement change data of the extension structures in the derived fracture.

With an increase in shear stress, the tension gash rotates while growing and extending. It rotates in the same direction as the shear stress and gradually diverges from the PDZ. For example, under the control of sinistral strike-slip in the study area, tension gashes rotated counterclockwise (Fig. 9). Fault rotation with strike-slip displacement is very common near the PDZ of strike-slip faults. According to various studies, the R shear generated in the early stages of shear strike-slip zone development has a similar rotation and gradually converges to the PDZ (Xiao et al., 2017).

Although tension gashes rotate as a whole, their rotational strength varies depending on the location of the fault. The shear strain gradually decreases as the distance from the PDZ increases. According to the shear strain value measured in Fig. 7, the strain is greater than 1.5 near the PDZ, while at both ends of STG, far away

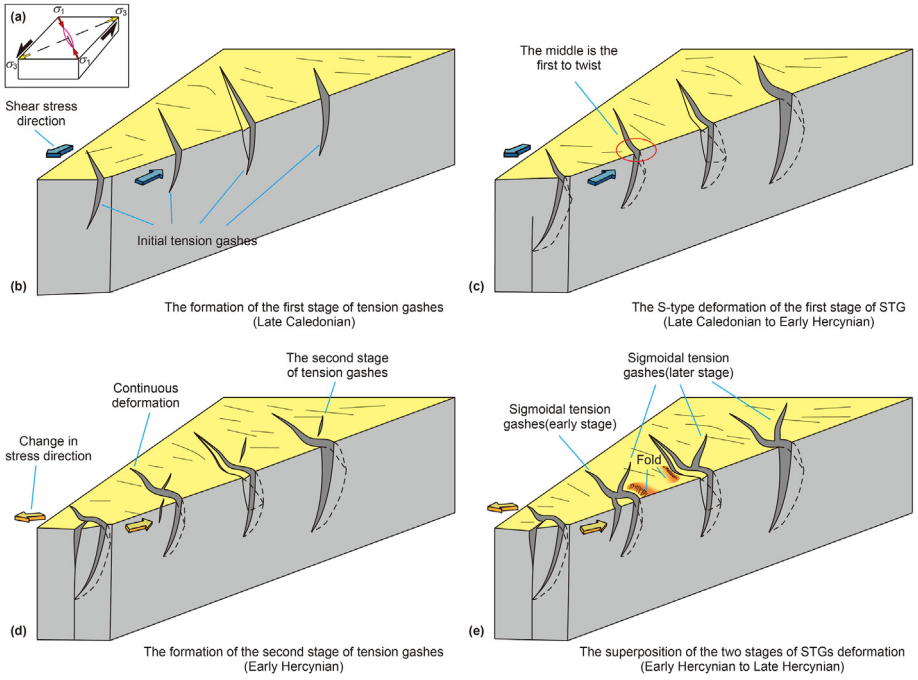

Fig. 9. Diagram of sigmoidal tension gashes (STGs) formation mechanism. (a) Stress mechanism of initial tension gashes formation. (b) Initial tension gashes formation stage and corresponding period. (c) S-type deformation and corresponding period of the first stage STG. (d) The second stage of tension gashes formation and its corresponding period. (e) Two STGs superimposed deformation stages and corresponding periods.

from the main displacement zone, the strain is mostly less than 1. It is found that the high-value area of STG strain is near the PDZ of the strike-slip fault, and the strain directions on both sides of the high-value area change. This phenomenon causes the STG to rotate counterclockwise, and the displacement produced by the rotation of the various parts is different. This displacement is larger near the PDZ and smaller away from the PDZ. Finally, S-shape geometry is generated.

Our research also revealed that in the Shunnan area, more than one stage of *en échelon* STGs has developed. A group of *en échelon* faults intersecting the STG forms a conjugate X-type pattern in the NE direction with a relatively small angle with the PDZ. These faults have a similar development direction and combination style to the R shear, which formed during the early stages of strike-slip faulting (Dooley and Schreurs, 2012; Chemenda et al., 2016; Xu et al., 2017). However, the plane and cross-sectional characteristics of this group of faults differ from those of R shears: (1) The faults in this group appear in pairs, displaying two faults with opposite dips and small grabens with tension characteristics in the cross-section. (2) This type of fault differs from shear faults because it has a high "penetrability" and can dislocate faults that have formed early in the process (Lin et al., 2011; Carpentier et al., 2012; Bewick et al., 2013). Affected by STGs formed in the early stage, they "merge" into the STGs instead of cutting through those that formed in the early stage. This is also consistent with the characteristics of tensional faults. (3) The azimuth of this fault group differs in several ways. The paired faults with earlier formation times, longer fault extensions, and larger openings between faults have smaller azimuths in this group of NE-trending *en échelon* faults in the study area (Figs. 4 and 5b). In contrast, the paired faults with later formation times, shorter fault extensions, and smaller openings between faults have larger azimuths (Figs. 4 and 5f). This indicates that faults rotate counterclockwise as they grow and develop, similar to the NW-trending STG. Based on the above characteristics, the NE-trending faults of this group had the same nature as the early NW-trending STG. The direction of the shear stress in the region did not change as the shear stress increased, and its stress components σ_1 and σ_3 continued to superimpose at the initial part of the STG to produce new tension gashes.

In summary, we believe that the evolution process of current STG can be divided into four stages (Fig. 9). The first stage occurred in the late Caledonian period, when the Tarim Basin and the Altyn Block in the southeast were in a post collision period of intense activity, and the stress was transferred to the Shunnan area, producing nearly NE-trending sinistral shearing. Under the influence of this action, the first stage tension gashes were formed, distributed in *en échelon* along the early strike-slip displacement zone (Fig. 9b). In the second stage, from the late Caledonian to early Hercynian period, the Altyn Block continued to collide, but the intensity of activity gradually weakened, and shear stress continued to occur in the Shunnan region. The initial fracture gradually underwent counterclockwise twisting deformation from the middle to both ends, ultimately forming a group of STGs (Fig. 9c). In the third stage, during the early Hercynian period, the activity of the Altyn Block gradually ceased, while the Tianshan Block in the northeast began to collide and compress. This tectonic movement generated a new stress field in the Shunnan area. Under the control of this stress, the second stage tension gashes formed. And intersects with the first stage STG at a certain angle (Fig. 9d). In the fourth stage, from early Hercynian to late Hercynian, the collision of the Tianshan Block continued. The growth and development of the second stage tension gashes connected the first stage STG, resulting in the structural current morphology of the two stages of STGs (Fig. 9e).

5.3. Relationship with oil and gas accumulation

The Shunnan area is close to the source rock in the Cambrian and has a good regional caprock (Zhen et al., 2015; Qi, 2016; Liu et al., 2021). The tectonic evolution of this area suggests that it has been a long-developed slope, making it a good spot for late hydrocarbon migration and accumulation (Wang et al., 2014b; Cao et al., 2019). Oil and gas are found in the upper and lower Yijianfang and Yingshan formations of the Ordovician; these are primarily sourced from the Manjiaer Depression (Sha et al., 2014; Huang, 2014; He et al., 2019). Many factors, such as structural fractures, hydrothermal dissolution transformation, and dolomitization, control the development of reservoirs, which are mainly dissolved carves, karst, and pores along the fractures (Zhao et al., 2012; Chen et al., 2015; You et al., 2018; Kang et al., 2020). The formation of large-scale effective reservoirs depends on the multi-stage development of strike-slip faults and their associated structures (Li et al., 2016). Different types of strike-slip-related structures exhibit different reservoir-forming rules and patterns. STGs are one of the most favorable locations for hydrocarbon accumulation because of the easy connection between source rocks and deep hydrothermal fluids, various types of reservoirs, and better locations for hydrocarbon charging.

Faults are important pathways for hydrocarbon migration. In the study area, there are primarily two types of fault development: STGs with tensile properties and deep strike-slip faults with shear properties (Fig. 11). The direction and relative size of fracture permeability are related to the direction and size of the principal stress at its location (Faulkner and Armitage, 2013). The maximum permeability tensor is typically parallel to the direction of the intermediate principal stress, whereas the minimum and intermediate permeability tensors are parallel to the directions of the minimum and maximum principal stresses, respectively (Faulkner and Armitage, 2013; Liu et al., 2020). This phenomenon shows that the difference in fracture properties can affect the difference in

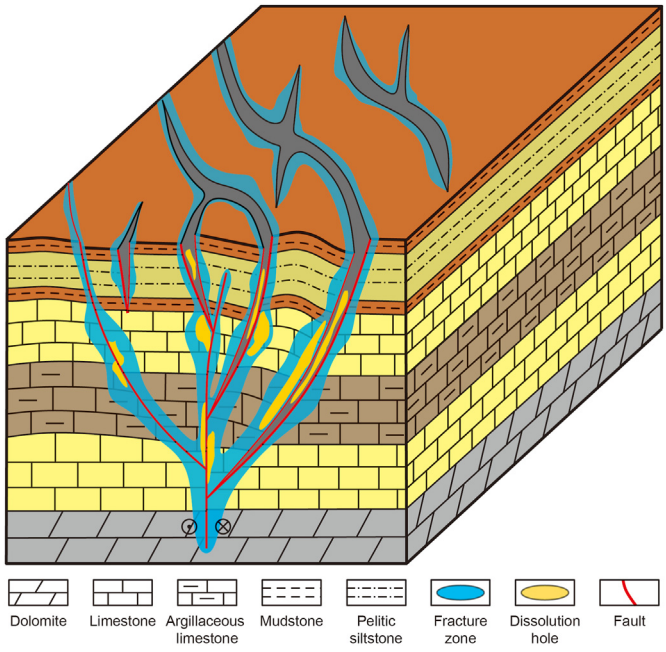

Fig. 11. Schematic illustration of sigmoidal tension gashes forming oil and gas reservoir. The fracture system formed by the early-stage strike-slip fault and the late-stage sigmoidal tension gashes. It is the paths of oil and gas transmission and accumulation. The oil and gas were transported upward along the strike-slip fault and aggregated in the pore-slit reservoirs modified by the faults.

permeability tensor and size. Therefore, STGs can provide various ways of transporting and storing hydrocarbons in strike-slip faults. Deep strike-slip faults can be used as vertical migration channels to connect the oil source or deep hydrothermal fluid to shallow formations in the study area. The STGs produced by the shallow tension–torsional stress field are crucial in the reconstruction of the surrounding strata. (1) First, the development of the faults induces fractures in the surrounding rocks, improving the physical parameters of these rocks. The development range of fractures controlled by strike-slip faults is 1.25–6.5 times the width of the core of the fault zone, and the development range and strength of the derived fractures in the tension-torsion section of the strike-slip faults are significantly greater than those in the translation section (Zhang et al., 2018). (2) Its strong strike-migration and transformation effect on the surrounding strata makes hydrothermal fluid filling easier. Liu et al. (2021) found that fluorite and calcite fill the fractures in the coring section of several wells in the Middle and Lower Ordovician strata of the Shunnan area, and the FeO and MnO contents in dolomite and calcite are high. Fluorite inclusions have a homogenization temperature of 165–175 °C, which is approximately 30 °C higher those that of the surrounding rocks and typical of hydrothermal fluids (Liu et al., 2021). Moreover, a cataclastic structure related to hydrothermal rupture was discovered, confirming the existence of hydrothermal fluids in the study area. Along the large and deep faults, deep acidic hydrothermal fluid flowed upward into the shallow carbonate strata (Jiao, 2017). Dissolution and cementation occur simultaneously in the relatively closed burial diagenetic environment, with fracture-cavity development and cementation zones at different locations, further transforming the pore fabric and space of the strata around the fault. The Querquke Formation in the Upper Silurian contains extremely thick mudstones (approximately 2000 m) with pure, dense lithology and strong compaction (Han et al., 2018). Once a reservoir is formed and hydrocarbon fluids are charged, these mudstones act as efficient cap rocks and form hydrocarbon accumulations.

6. Conclusions

(1) We identified the large scale STGs in the buried strata of the Shunnan area. They were assembled and arranged in an en échelon pattern in the plane view. A single tension gash has a horizontally bending "S"-shape. Several groups of *en échelon* STGs can form in areas of high stress, and the direction of early STGs differs from that of late STGs, which is the result of rotation along the shear stress direction during formation.

(2) STGs are characterized by high intermediate stress and low stress at both ends, and the degree of shallow deformation is greater than that of deep deformation. The degree of deformation is affected by the scale and opening degree of the STG and shear stress. Tension gashes with a large scale and opening degree are not easily sheared or dislocated, and the degree of deformation is high. Tension gashes with a small scale and opening degree are easily sheared and dislocated, and the degree of deformation is small.

(3) STGs provide favorable conditions for oil and gas accumulation because of the efficient connection between the source rocks and reservoir, good migration and sealing capability, and excellent reservoir development. The shallow strike-slip fault can improve the physical parameters of the surrounding strata by generating structural fractures and hydrothermal dissolution and cementation, which is conducive to large-scale oil and gas accumulation.

Declaration of competing interest

The authors declare that they have no known competing financial interests or personal relationships that could have appeared to influence the work reported in this paper.

Acknowledgments

Thanks to the Northwest Oilfield Branch, SINOPEC, for providing the seismic data. We thank Dr. Yi-Duo Liu of University of Houston, Ying-Chang Cao and Fang Hao of China University of Petroleum (East China) for their constructive suggestions of this manuscript. We also thank two anonymous reviewers for their comments that helped us to improve the manuscript. This research is jointly supported by the National Natural Science Foundation of China (No. 42272155), the Strategic Priority Research Program of the Chinese Academy of Sciences (No. XDA14010301), the Science Fund for Creative Research Groups of the National Natural Science Foundation of China (Grant No. 41821002) and National Natural Science Foundation of China (No.41702138).

References

Beach, A., 1975. The geometry of en-echelon vein arrays. Tectonophysics 28, 245–263. https://doi.org/10.1016/0040-1951(75)90040-2.

Bewick, R.P., Kaiser, P.K., Bawden, W.F., Bahrani, N., 2013. DEM simulation of direct shear: 1. rupture under constant normal stress boundary conditions. Rock Mech. Rock Eng. 47 (5), 1647–1671. https://doi.org/10.1007/s00603-013-0490-8.

Cao, Y.H., Wang, S., Zhang, Y.J., Yang, M., Yan, L., Zhao, Y.M., Zhang, J.L., Wang, X.D., Zhou, X.X., Wang, H.J., 2019. Petroleum geological conditions and exploration potential of Lower Paleozoic carbonate rocks in Gucheng area, Tarim Basin, China. Petrol. Explor. Dev. 46 (6), 1165–1181. https://doi.org/10.1016/S1876-3804(19)60271-5.

Carpentier, S.F.A., Green, A.G., Langridge, R., Boschetti, S., Doetsch, J., Abächerli, A.N., Horstmeyer, H., Finnemore, M., 2012. Flower structures and riedel shears at a step over zone along the alpine fault (New Zealand) inferred from 2-D and 3-D GPR images. J. Geophys. Res. 117, 1–6. https://doi.org/10.1029/2011JB008749.

Cembrano, J., González, G., Arancibia, G., Ahumada, I., Olivares, V., Herrera, V., 2005. Fault zone development and strain partitioning in an extensional strike-slip duplex: a case study from the Mesozoic Atacama fault system, Northern Chile. Tectonophysics 400 (1–4), 105–125. https://doi.org/10.1016/j.tecto.2005.02.012.

Chemenda, A.I., Cavalié, O., Vergnolle, M., Bouissou, S., Delouis, B., 2016. Numerical model of formation of a 3-D strike-slip fault system. C. R. Geosci. 348 (1), 61–69. https://doi.org/10.1016/j.crte.2015.09.008.

Chen, Y.Q., Guan, B.Z., Xiong, Y.X., Kang, Q., 2015. Compound cap rocks and slide faults controlling mechanism on reservoir and reserves: an example on Lower Ordovician dolostones exploration in Manxi-Gucheng area, Tarim Basin. Nat. Gas Geosci. 26 (7), 1268–1276. doi:10.11764/j.issn.1672-1926.2015.07.1268.(in Chinese).

Deng, S., Li, H.L., Zhang, Z.P., Wu, X., Zhang, J.B., 2018a. Characteristics of differential activities in major strike-slip fault zones and their control on hydrocarbon enrichment in Shunbei area and its surroundings. Tarim Basin. Oil Gas Geol. 39 (5), 878–888. https://doi.org/10.11743/ogg20180503 (in Chinese).

Deng, S., Li, H.L., Zhang, Z.P., Zhang, J.B., Yang, X., 2018b. Structural characterization of intracratonic strike-slip faults in the central Tarim Basin. AAPG Bull. 103 (1), 109–137. https://doi.org/10.1306/06071817354.

Dooley, 1994. Geometries and Kinematics of Strike-Slip Fault Systems: Insights from Physical Modelling and Field Studies. R. Holloway Univ. London.

Dooley, T.P., Schreurs, G., 2012. Analogue modelling of intraplate strike-slip tectonics: a review and new experimental results. Tectonophysics 574 (575), 1–71. https://doi.org/10.1016/j.tecto.2012.05.030.

Dorigo, M., Maniezzo, V., Colorni, A., 1996. Ant system: optimization by a colony of cooperating agents. IEEE Trans. Cybern. 26 (1), 29–41. https://doi.org/10.1109/3477.484436.

Tóth, E., Hrabovszki, E., Steinbach, G., Schubert, F., 2019. Quantitative estimation of shear strain and volume change using sigmoidal tension gashes. Földt. Közl. 148 (4), 367–380. https://doi.org/10.23928/foldt.kozl.2018.148.4.367.

Faulkner, D.R., Armitage, P.J., 2013. The effect of tectonic environment on permeability development around faults and in the brittle crust. Earth Planet Sci. Lett. 375 (8), 71–77. https://doi.org/10.1016/j.epsl.2013.05.006.

Fossen, H., 2010. Structural geology: shear zones and mylonites. Structural Geology 285–310.

Fossen, H., Cavalcante, G., 2017. Shear zones – a review. Earth Sci. Rev. 171, 434–455. https://doi.org/10.1016/j.earscirev.2017.05.002.

Han, X.Y., Tang, L.J., Cao, Z.C., Wei, H.D., Fu, C.Y., 2018. Characteristics and formation mechanism of composite flower structures in northern slope of Tazhong Uplift,

Tarim Basin. Earth Sci. 43 (2), 525–537. doi:10.3799/dqkx.2017.600. (in Chinese).
Han, J.F., Su, Z., Chen, L.X., Guo, D.S., Zhang, Y.T., Ji, Y.G., Zhang, H.F., Yuan, J.Y., 2019. Reservoir-controlling and accumulation-controlling of strike-slip faults and exploration potential in the platform of Tarim Basin. Acta Pet. Sin. 40 (11), 1296–1310. doi:10.7623/syxb201911002. (in Chinese).
He, D.F., Jia, C.Z., De, S., Zhang, C.J., Meng, Q.R., Shi, X., 2005. Formation and evolution of polycyclic superimposed Tarim Basin. Oil Gas Geol. 26 (1), 64–77. doi:10.1016/j.molcatb.2005.02.001. (in Chinese).
He, Z.L., Yun, L., You, D.H., Peng, S.T., Zhang, H., Wang, K.N., Qian, Y.X., Jiao, C.L., Zhang, J.B., 2019. Genesis and distribution prediction of the ultra-deep carbonate reservoirs in the transitional zone between the Awati and Manjiaer depressions, Tarim Basin. Earth Sci. Front. 26 (1), 13–21. doi:10.13745/j.esf.sf.2018.12.20. (in Chinese).
Huang, T.Z., 2014. Structural interpretation and petroleum exploration targets in northern slope of middle Tarim Basin. Pet. Geol. Exp. 36 (3), 257–267. doi:10.11781/sysydz201403257. (in Chinese).
Huang, C.X., Xia, X.H., Shen, W.P., 1998. Measurement and back analysis on the initial rock stress field around the faults. J. Shanghai Jiao Tong Univ. (Sci.) 32 (12), 57–61. doi:10.16183/j.cnki.jsjtu.1998.12.013. (in Chinese).
Jia, C.Z., Ma, D.B., Yuan, J.Y., Wei, G.Q., Yang, M., Yan, L., Tian, F.L., Jiang, L., 2021. Structural characteristics, formation & evolution and genetic mechanisms of strike-slip faults in the Tarim Basin. Nat. Gas. Ind. 41 (8), 81–91. doi:10.3787/j.issn.1000-0976.2021.08.008. (in Chinese).
Jiao, F.Z., 2017. Significance of oil and gas exploration in NE strike-slip fault belts in Shuntuoguole area of Tarim Basin. Oil Gas Geol. 38 (5), 831–839. doi:10.11743/ogg20170501. (in Chinese).
Jiao, F.Z., 2018. Significance and prospect of ultra-deep carbonate fault-karst reservoirs in Shunbei area, Tarim Basin. Oil Gas Geol. 39 (2), 207–216. doi:10.11743/ogg20180201. (in Chinese).
Kang, Y.Z., 2018. The resource potential and exploration for oil and gas in the Tarim Basin. Pet. Sci. Bull. 3 (4), 369–375. doi:10.3969/j.issn.2096-1693.2018.04.033. (in Chinese).
Kang, R.D., Meng, W.B., Xiao, C.H., 2020. Formation mechanisms and development models of dolomite reservoirsin ordovician Yingshan Formation in Shunnan area, Tarim Basin. Pet. Geol. Exp. 42 (6), 900–909. doi:10.11781/sysydz202006900. (in Chinese).
Lajtai, E.Z., 1969. Mechanics of second order faults and tension gashes. Geol. Soc. Am. Bull. 80 (11), 2253–2272.
Li, K.B., Yun, L., Pu, R.H., Cao, Z.C., 2016. Relationship between volcanic activity and fault, hydrothermalism in Shunnan-1 3D well zone in Tadong area, Tarim Basin. Prog. Geophys. 31 (5), 1934–1946. doi:10.6038/pg20160507. (in Chinese).
Li, P.J., Chen, H.H., Tang, D.Q., Cao, Z.C., Lu, Z.Y., Su, A., Wei, H.D., 2017. Coupling relationship between NE strike-slip faults and hypogenic karstification in middle-lower ordovician of Shunnan area, Tarim Basin, north-west China. Earth Sci. 42 (1), 93–104. doi:10.3799/dqkx.2017.007. (in Chinese).
Li, W., Meng, M.F., Chen, X.P., Zhang, T.J., Yang, H.F., Niu, C.M., Wu, Z.P., Feng, J.W., 2021. Quantitative characterization of extension and compression derived from bending strike-slip faults and their petroleum geological significance of the eastern Bohai Sea. J. China Univ. Pet. Ed. Nat. Sci. (Edition of Natural Science) 45 (5), 23–32. doi:10.3969/j.issn.1673-5005.2021.05.003. (in Chinese).
Lin, C.S., Li, S.T., Liu, J.Y., Qian, Y.X., Luo, H., Chen, J.Q., Peng, L., Rui, Z.F., 2011. Tectonic framework and paleogeographic evolution of the Tarim Basin during the Paleozoic major evolutionary stages. Acta Pet. Sin. 27 (1), 210–218. doi:10.1134/S002449021101007X. (in Chinese).
Lin, B., Yun, L., Li, H.Y., Xiao, C.Y., Zhang, X., Liao, M.H., Han, J., Wang, P., Xu, X.C., 2021. Spatial structure of Shunbei No. 5 strike-slip fault and its relationship with oil and gas reservoirs in the Tarim Basin. Oil Gas Geol. 42 (6), 1344–1353+1400. doi:10.11743/ogg20210609. (in Chinese).
Lisle, R.J., 2013. Shear zone deformation determined from sigmoidal tension gashes. J. Struct. Geol. 50, 35–43. https://doi.org/10.1016/j.jsg.2012.08.002.
Liu, H.B., Cui, S., Meng, Y.F., Deng, H., Han, H., 2020. Micro-mechanical structure and mechanical properties of fractured carbonate rock. Special Oil Gas Reservoirs 27 (1), 155–161. doi:10.3969/j.issn.1006-6535.2020.01.023. (in Chinese).
Liu, J., Chen, Q.L., Wang, P., You, D.H., Xi, B.B., Gong, H.N., 2021. Characteristics and main controlling factors of carbonate reservoirs of Middle-Lower Ordovician, Shunnan area, Tarim Basin. Pet. Geol. Exp. 43 (1), 23–33. doi:10.11781/sysydz202101023. (in Chinese).
Liu, Y., Suppe, J., Wang, X., Cao, Y.C., Hao, F., Liu, Y.D., Wu, K.Y., Cao, Z.C., Wei, H.H., 2023. Linkage and formation of strike-slip faults in deep basins and its implications for petroleum accumulation: a case study from the Shunbei area of the Tarim Basin, China. AAPG Bull. 107 (2), 331–355. https://doi.org/10.1306/11142220110.
Liu, Z., Li, S.Z., Suo, Y.H., Bukhari, S.W.H., Ding, X.S., Zhou, J., Wang, P.C., Cheng, H.H., Somerville, I., 2023. Evolution of pull-apart basins with overlapping NE-trending strike-slip fault systems in the northern South China Sea margin: Insight from numerical modeling. Tectonophysics 846, 229679. https://doi.org/10.1016/j.tecto.2022.229679.
Mann, P., 2007. Global catalogue, classification and tectonic origins of restraining and releasing bends on active and ancient strike-slip fault systems. Geological Society, London, Special Publications 290 (1), 13–142. https://doi.org/10.1144/SP290.2.
Means, W.D., 1984. Shear zones of types I and II and their significance for reconstruction of rock history. Geol. Soc. Am. Abstr. 16, 50.
Means, W.D., 1995. Shear zones and rock history. Tectonophysics 247, 157–160. https://doi.org/10.1016/0040-1951(95)98214-H.
Qi, L.X., 2016. Oil and gas breakthrough in ultra-deep ordovician carbonate formations in Shuntuoguole uplift, Tarim Basin. China Pet. Explor. 21 (3), 38–51. doi:10.3969/j.issn.1672-7703.2016.03.004. (in Chinese).
Qiu, H., Deng, S., Cao, Z.C., Yin, T., Zhang, Z.P., 2019. The evolution of the complex anticlinal belt with crosscutting strike-slip faults in the central Tarim Basin, NW China. Tectonics 38 (6), 2087–2113. https://doi.org/10.1029/2018TC005229.
Ramsay, J.G., Graham, R.H., 1970. Strain variation in shear belts. Can. J. Earth Sci. 7 (3), 786–813. https://doi.org/10.1139/e70-078.
Ramsay, J.G., Huber, M.I., 1983. The techniques of modern structural geology. In: Strain Analysis, vol. 1. Academic Press, London. https://doi.org/10.1016/0012-8252(86)90038-3.
Ren, J.Y., Zhang, J.X., Yang, H.Z., Hu, D.S., Zhang, Y.P., 2011. Analysis of fault systems in the central uplift, Tarim Basin. Acta Pet. Sin. 27 (1), 219–230 (in Chinese).
Rispoli, R., 1981. Stress fields about strike-slip faults inferred from stylolites and tension gashes. Tectonophysics 75 (3–4), T29–T36. https://doi.org/10.1016/0040-1951(81)90274-2.
Sha, X.G., Ma, Q.Y., Lu, H.T., Li, X.Y., Zhu, X.X., 2014. Hydrocarbon accumulation and main controlling factors of ordovician reservoir in guchengxu uplift, Tarim Basin. Mar. Origin Pet. Geol. 19 (2), 15–22. doi:10.3969/j.issn.1672-9854.2014.02.003. (in Chinese).
Shen, H.C., Cheng, F.Y., Zhao, Y.Z., Zhang, J.G., Xia, Y.B., 2008. Study on influence of faults on geostress by measurement data and numerical simulation. Chin. J. Rock Mech. Eng. 27 (S2), 3985–3990 (in Chinese).
Smith, J.V., Durney, D.W., 1992. Experimental formation of brittle structural assemblages in oblique divergence. Tectonophysics 216 (3–4), 235–253. https://doi.org/10.1016/0040-1951(92)90399-Q.
Tang, L.J., 1994. Evolution and tectonic patterns of Tarim Basin. Earth Sci. J. China Univ. Geosci. 19 (6), 742–754 (in Chinese).
Vitale, S., Mazzoli, S., 2008. Heterogeneous shear zone evolution: the role of shear strain hardening/softening. J. Struct. Geol. 30 (11), 1383–1395. https://doi.org/10.1016/j.jsg.2008.07.006.
Wang, J., Li, Y., Gan, L., 2013. Fracture characterization based on azimuthal anisotropy of ant-tracking attribute volumes. Oil Geophys. Prospect. 48 (5), 763–769. doi:10.13810/j.cnki.issn.1000-7210.2013.05.022. (in Chinese).
Wang, Q.H., Yang, H.J., Wang, R.J., Li, S.Y., Deng, X.L., Li, Y., Chang, L.J., Wan, X.G., Zhang, Y.T., 2021. Discovery and exploration technology of fault-controlled large oil and gas fields of ultra-deep formation in strike slip fault zone in Tarim Basin. China Pet. Explor. 26 (4), 58–71. doi:10.3969/j.issn.1672-7703.2021.04.005. (in Chinese).
Wang, B.C., Liu, J., Ma, L.W., Li, Z.J., Zhong, X.B., 2014a. Forward modeling for seismic response characteristics of the fracture-cavity Ordovician reservoir in Shunnan area of central Tarim Basin. Geophys. Prospect. Pet. 53 (3), 344–350+359. doi:10.3969/j.issn.1000-1441.2014.03.013. (in Chinese).
Wang, T.G., Song, D.F., Li, M.J., Yang, C.Y., Ni, Z.Y., Li, H.L., Cao, Z.C., Zhang, B.S., Feng, Z.H., 2014b. Natural gas sourceand deep gas exploration potential of the Ordovician Yingshan Formation in the Shunnan-Gucheng region. Tarim Basin. Oil Gas Geol. 35 (6), 753–762. https://doi.org/10.11743/ogg20140602 (in Chinese).
Wang, R.J., Wang, X., Deng, X.L., Zhang, Y.T., Yuan, J.Y., Xie, Z., Li, T., Luo, X., Ma, X.P., 2021. Control effect of strike-slip faults on carbonate reservoirs and hydrocarbon accumulation: a case study of the northern depression in the Tarim Basin. Nat. Gas. Ind. 41 (3), 10–20. doi:10.3787/j.issn.1000-0976.2021.03.002. (in Chinese).
Wang, Z.Y., Gao, Z.Q., Fan, T.L., Zhang, H.H., Yuan, Y.X., Wei, D., Qi, L.X., Yun, L., Karubandika, G.M., 2022. Architecture of strike-slip fault zones in the central Tarim Basin and implications for their control on petroleum systems. J. Pet. Sci. Eng. 213, 110432. https://doi.org/10.1016/j.petrol.2022.110432.
Woodcock, N.H., Fischer, M., 1986. Strike-slip duplex. J. Struct. Geol. 8 (7), 725–735. https://doi.org/10.1016/0191-8141(86)90021-0.
Xiao, Y., Wu, G.H., Lei, Y.L., Chen, T.T., 2017. Analogue modeling of through-going process and development pattern of strike-slip fault zone. Petrol. Explor. Dev. 44 (3), 340–348. https://doi.org/10.11698/PED.2017.03.03.
Xu, Z.Q., Li, H.B., Tang, Z.M., Qi, X.X., Li, H.Q., Cai, Z.H., 2011. The transformation of the terrain structures of the Tibet Plateau through large-scale strike-slip faults. Acta Pet. Sin. 27 (11), 3157–3170 (in Chinese).
Xu, S.H., Peng, H., Angel, F., Chen, S.P., Wu, X.D., 2017. The similarity between riedel shear patterns and strike-slip basin patterns. Geol. Rev. 63 (2), 287–301. doi:10.16509/j.georeview.2017.02.003. (in Chinese).
You, D.H., Han, J., Hu, W.X., Chen, Q.L., Cao, Z.C., Xi, B.B., Lu, Z.Y., 2018. Characteristics and genesis of dolomite reservoirs in the Yingshan formation of well SN501 in the Tarim Basin. Acta Sedimentol. Sin. 36 (6), 1206–1217. doi:10.14027/j.issn.1000-0550.2018.092. (in Chinese).
Yun, L., Cao, Z.C., 2014. Hydrocarbon enrichment pattern and exploration potential of the Ordovician in Shunnan area, Tarim Basin. Oil Gas Geol. 35 (6), 788–797. doi:10.11743/ogg20140606. (in Chinese).
Zhang, J.B., Zhang, Z.P., Wang, B.F., Deng, S., 2018. Development pattern and prediction of induced fractures from strike-slip faults in Shunnan area, Tarim Basin. Oil Gas Geol. 39 (5), 955 963+1055. doi:10.11743/ogg20180510. (in Chinese).
Zhao, J.Z., Jia, C.Z., 2002. Structural characteristics and tectonic evolution of the awati-Manjia'er ridge, the Tarim Basin. Geol. Rev. 48 (1), 68–73. doi:10.16509/j.georeview.2002.01.012. (in Chinese).
Zhao, W.Z., Shen, A.J., Hu, S.Y., Pan, W.Q., Zheng, J.F., Qiao, Z.F., 2012. Types and distributional features of Cambrian-Ordovician dolostone reservoirs in Tarim Basin, northwestern China. Acta Petrol. Sin. 28 (3), 758–768 (in Chinese).

Zhen, S.J., Tang, L.J., Li, Z.J., Li, M., Cao, Z.C., Yang, S.J., 2015. The characteristics, formation and petroleum geology significance of the strike-slip fault system in Shunnan area, northern slope of Tazhong uplift. Nat. Gas Geosci. 26 (12), 2315–2324. doi:10.11764/j.issn.1672-1926.2015.12.2315. (in Chinese).

Zhou, W., Yin, T.J., Zhang, Y.C., Li, W.Q., Wang, D.D., 2015. Application of ant tracking technology to fracture prediction: a case study from Xiagou Formation in Qingxi Oilfield. Northwest Oil Gas Explor 27 (6), 111–118 (in Chinese).

Zhu, X., Zhu, H.T., Chen, H.H., Qi, L., Li, P.J., Yun, L., 2016. Characterization of hypogenic karst systems in the middle-lower ordovician of Shun-nan area, Tarim Basin. Oil Gas Geol. 37 (5), 653–662. doi:10.11743/ogg20160505. (in Chinese).